Experimental Study of the Multipolar Vortex Instability

Christophe Eloy, Patrice Le Gal, and Stéphane Le Dizès

Institut de Recherche sur les Phénomènes Hors Équilibre, CNRS UMR 6594, Marseille, France

The instability of a vortex subjected to a stationary dipolar or tripolar constraint is studied experimentally by using a rotating deformable cylinder on which two or three rollers are applied. As the Reynolds number and the aspect ratio of the cylinder are varied, different modes of instability are observed and their wavelength and frequency are compared to theoretical predictions. Secondary instability and cyclic breakup are also evidenced in the elliptic geometry.

One of the most challenging issues of fluid turbulence is to understand the dynamics of fine-scale structures in order to give an insight into the global properties of the flows. Recently, intense vortical structures have been evidenced by experimental and numerical studies [1]. When perturbed by the surrounding turbulent flow, they eventually undulate, split, form strands, and burst. This complex dynamical behavior has been associated with the presence of Kelvin modes [2]. However, no convincing mechanism has been proposed to explain the apparition of such modes. In this Letter, we argue that the *elliptic instability* [3] whose proper modes are precisely combinations of Kelvin modes [4] is a good candidate. In this prospect, the ellipticity of the vortex streamlines [5] which is due to the nonaxisymmetry of the surrounding turbulent flow would provide the source of instability.

Gledzer *et al.* [6] were the first to study experimentally the elliptic instability. They used a rigid cylinder of elliptic cross section filled with water which was sharply stopped after solid body rotation was reached. During the transient decay of the flow, they observed the development of the elliptic instability. In addition to the limited time during which instability was observed, the main inconvenience of their experiment was that a competitive centrifugal instability could grow near the wall. This defect was avoided by Malkus and Waleffe [7] who used the boundary to drive the flow inside a deformable cylinder. In this paper, experiments are carried out with a similar setup. New results are obtained in the elliptic geometry, and the instability is generalized to azimuthal symmetries of higher order.

The core of the experiment is a transparent plastic extruded cylinder of radius $R = 2.75$ cm and variable length $H = 8-22$ cm. The small thickness of its wall (0.5 mm) allows its deformation with two or three rollers parallel to the axis, as shown in Fig. 1. This deformed cylinder is rotated by a 300 W variable speed electric motor at a chosen angular speed $\Omega = 0.5-10$ rad s^{-1}. The cylinder is filled with water seeded by anisotropic particles (kalliroscope). A laser sheet is formed in a plane containing the cylinder axis for visualization. As emphasized by [8], this visualization technique does not permit one to have insight into the velocity field. However, it allows an unambiguous measurement of wavelengths and frequencies of modes appearing in the cylinder.

When the cylinder is rotated and after the transient phase of spin-up, the basic flow is approximatively described, in cylindrical coordinates (r, θ, z), by the stream function:

$$\psi(r, \theta) = -\frac{1}{2} r^2 + \frac{\varepsilon}{n} r^n \sin(n\theta), \qquad (1)$$

where ε measures the deformation of the streamlines (ε is the eccentricity of the ellipses for $n = 2$) and n is the degree of azimuthal symmetry of the flow or equivalently the number of rollers deforming the elastic cylinder (see Fig. 2). Here, the variables are nondimensionalized by using the characteristic length R and time Ω^{-1}. The position of the rollers in the experiment is such that the deformation of the streamlines is $\varepsilon \approx 0.10$ for $n = 2$ and $\varepsilon \approx 0.12$ for $n = 3$. The outer streamline of the flow, solution of $\psi(r, \theta) = -\frac{1}{2}$, corresponds to the cylinder boundary [9]. The stream function (1) provides a two-dimensional flow of constant vorticity with an n-fold symmetry which is a generalization of the elliptical flow. Its unstable character with respect to short wavelength perturbations was shown in [10]. By using global techniques [4,6], these results were recently extended to larger wavelengths for a Rankine vortex in Ref. [11], where, in particular, the viscous selection process and the spatial structure of the most unstable perturbations were determined. This analysis can be adapted to the flow in a deformable cylinder. The main ideas of the theory are the following.
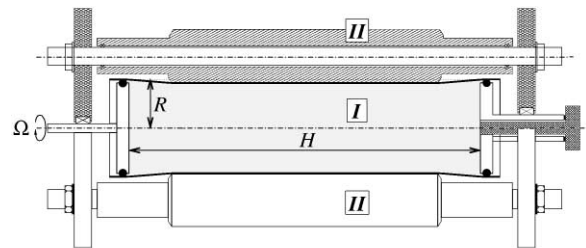

FIG. 1.   Experimental setup: (I) plastic elastic cylinder filled with water; (II) rollers.
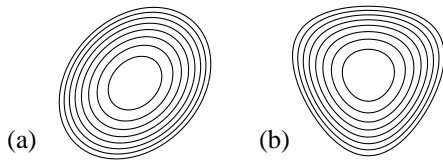
FIG. 2.   Streamlines of the flow given by (1), with $\varepsilon = 0.25$, and (a) $n = 2$ and (b) $n = 3$.

For axisymmetric flow ($\varepsilon = 0$), Kelvin modes can be superimposed linearly to the basic flow. Their velocity field can be written as $\mathbf{v}(r, \theta, z, t) = \mathbf{U}(r)e^{i(kz + m\theta - \omega t)}$, with k the axial wave number, m the azimuthal wave number, and ω the frequency. These kelvin modes are marginally stable for an axisymmetric and inviscid flow. In the limit of small deformation ε, Kelvin modes still exist. Moreover, two Kelvin modes can resonate if they have same k, same ω, and have azimuthal wave numbers m_1 and m_2, such that $m_2 - m_1 = n$. This resonance can be interpreted as a triad resonance of two Kelvin modes and the intrinsic "mode" of the deformation satisfying $[k, m, \omega] = [0, n, 0]$. A calculation of the growth rates shows that all possible resonances are unstable. However, particular combinations of Kelvin modes are significantly more amplified than others. These combinations are named *principal modes* and noted (m_1, m_2, i), where i is an integer which is an increasing function of the resonant wave number k. Frequencies and axial wave numbers of a few principal modes are provided in Table I. For an inviscid flow and an infinite cylinder, all principal modes have approximatively the same growth rate [11]. The selection is mainly due to viscosity which tends to damp the large wave number modes. Contrary to [11], both boundary layer and volume viscous effects are considered in the analysis. Figure 3 plots the theoretical marginal stability curves of all principal modes in the (k, Re) plane for the elliptic deformation ($n = 2$), where Re is the Reynolds number defined as $\Omega R^2/\nu$, with ν the kinematic viscosity. This figure shows that all modes are stabilized by viscosity for low Re. Above a critical Reynolds number, $\text{Re}_c = 435$, the first principal mode $(-1, 1, 1)$ becomes unstable. For larger Re, other modes of different azimuthal structure and different critical wave numbers k can also be destabilized.

TABLE I.   Theoretical prediction of frequency ω_{th} and axial wave number k_{th} of few principal modes (for inviscid flow and infinite cylinder) compared to experimental measurements ω_{exp} and k_{exp}.

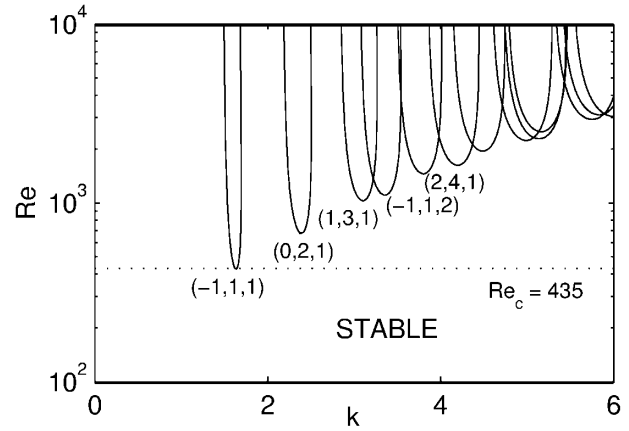| n	Mode	ω_{th}	ω_{exp}	k_{th}	k_{exp}
2	$(-1, 1, 1)$	0.000	0.00	1.579	1.6
2	$(-1, 1, 2)$	0.000	0.00	3.286	3.4
2	$(1, 3, 1)$	2.044	2.0	3.035	3.1
3	$(-1, 2, 1)$	0.656	0.65	3.674	3.7
3	$(0, 3, 1)$	1.608	1.5	5.185	5.0

FIG. 3.   Theoretical marginal stability curve of the elliptic instability for an infinite cylinder and $\varepsilon = 0.1$.

For a finite container, the principal modes are stationary waves, constituted by the superposition of two counterpropagative waves. There is an additional constraint due to boundary conditions on the end disks which selects a discrete set of axial wave numbers given by $k = l\pi R/H$, l being an integer. This constraint discards a large number of modes. The shaded areas in Fig. 7a below show the most unstable mode in the $(H/R, \text{Re})$ space of experimental control parameters. The mechanism of selection by viscosity and aspect ratio is similar for a triangular deformation (see Fig. 7b).

The experimental observations are the following. In both cases ($n = 2$ and $n = 3$), when the elastic cylinder is rotated, the fluid is first spun-up. Solid body rotation is
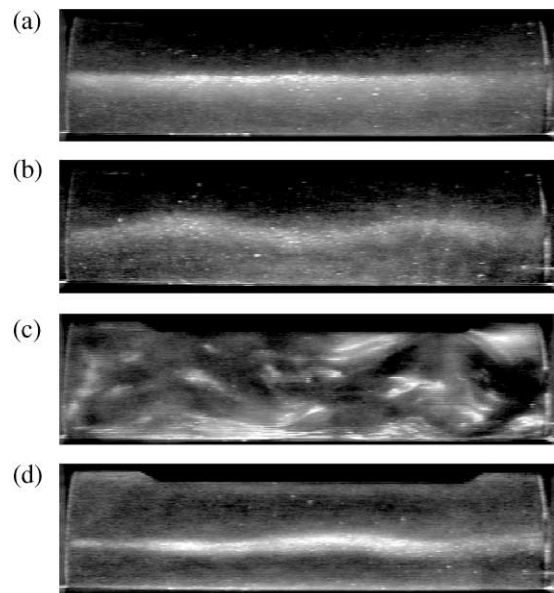

FIG. 4.   Four successive images of the flow for $n = 2$, Re = 5000, $H/R = 7.96$, and (a) $\Omega t = 294$, solid body rotation; (b) $\Omega t = 715$, appearance of mode $(-1, 1, 1)$; (c) $\Omega t = 943$, vortex breakup; (d) $\Omega t = 1113$, relaminarization.

reached after a time of order 6 to 25 rotations (Fig. 4a). If Re is above threshold, the multipolar instability develops and a mode appears in the cylinder (Fig. 4b). Since the characteristic time of this growth is at least 10 times larger than the spin-up time, the multipolar instability properties should not be affected by the transient regime. For Re $\gtrsim 4000$ and for elliptic deformation ($n = 2$), the mode grows until it breaks down into small scales (Fig. 4c). This disordered state is not maintained by the rotation of the cylinder. It eventually evolves back to solid body rotation by a relaminarization process through viscous dissipation of the small scales (Fig. 4d). The reestablishment of solid body rotation allows anew the development of the multipolar instability and so on. A cycle of instability–disorder–relaminarization then takes place, as already reported by Malkus and Waleffe [7]. However, contrary to what they apparently observed, for Re sufficiently close to threshold, the unstable mode grows and reaches a saturation state which remains forever (at least for 1000 rotations).

For these low Reynolds numbers, in agreement with the theory, the aspect ratio of the cylinder can be used to se-
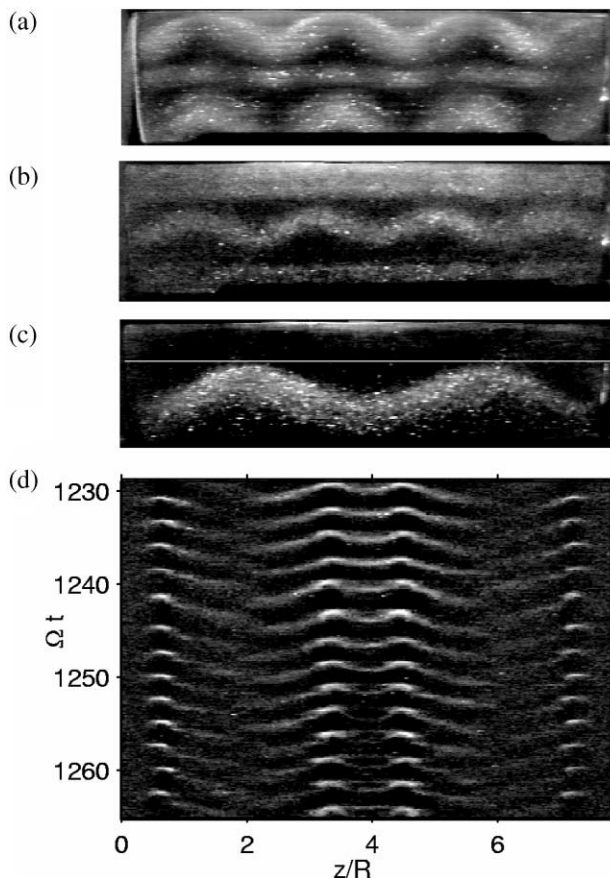
lect a preferential mode. This selection process is illustrated in Fig. 5, for $n = 2$. Depending on the length of the cylinder, three different modes were observed for the same Reynolds number. Each is characterized by a specific axial wavelength and frequency. Their wavelengths λ are determined by counting the number of identical structures along the cylinder (Figs. 5a–5c): $H = 3.5\lambda$, 4λ, and 2λ, respectively. Similarly, the mode frequencies are measured from spatiotemporal diagrams (see examples below). Both wavelengths and frequencies are in good agreement with theoretical predictions, as shown in Table I. Note that the primary modes associated with Figs. 5b and 5c are steady. This is in agreement with the prediction for the modes $(-1, 1, i)$.

A fast dynamics superimposed to the saturated state $(-1, 1, 1)$ has also been evidenced. It is likely to be an observation of the secondary instability revealed in [12], which is associated with a triad resonance of the principal mode $(-1, 1, 1)$ and two modes of azimuthal wave numbers $m = 2$ and 3. The periodic and pulsing character of this fast dynamics is shown in Fig. 5d where a spatiotemporal diagram is constructed by extracting a horizontal video line in each image of the video sequence. The measured frequency is $\omega = 2.3\Omega$, which is very close to the value 2.27 predicted by [12]. It is worth mentioning that, for Re $\lesssim 4000$, we have observed this secondary instability to saturate, without breakup of the vortex.

For triangular deformations of the cylinder, similar experiments have been carried out. For small aspect ratios, two different modes have been evidenced. Figure 6 displays visualizations of the flow and associated spatiotemporal diagrams for $H/R = 3.4$ and 3.8 and Re = 1200. The measurements of wavelengths and frequencies given in Table I show good agreement with our theoretical

FIG. 5.   Visualizations of the flow for $n = 2$, Re = 2500, and (a) $H/R = 7.13$; (b) 7.49, (c) 7.96. It corresponds, respectively, to the principal modes $(1, 3, 1)$, $(-1, 1, 2)$, and $(-1, 1, 1)$. The spatiotemporal diagram (d) shows the fast dynamics superimposed to the mode $(-1, 1, 1)$. The horizontal line in (c) shows which line has been extracted to construct (d).
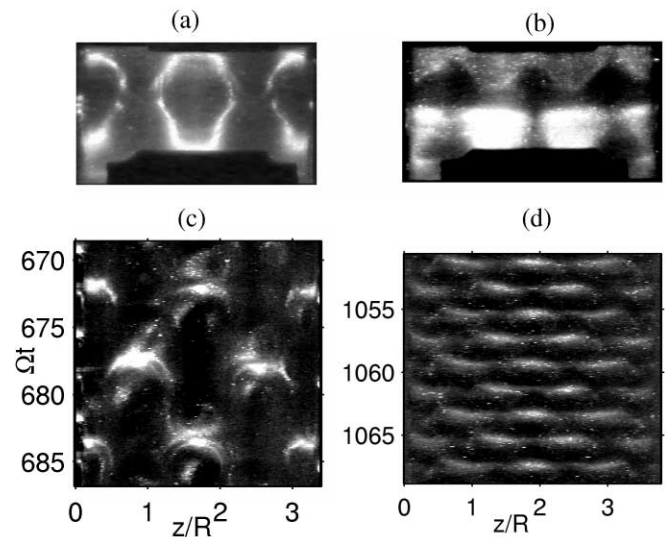

FIG. 6.   Visualization of the modes $(-1, 2, 1)$ (a) and $(0, 3, 1)$ (b), together with their spatiotemporal diagrams (c, d). The experimental parameters are $n = 3$, Re = 1200, and $H/R = 3.4$ (a) and 3.8 (b).
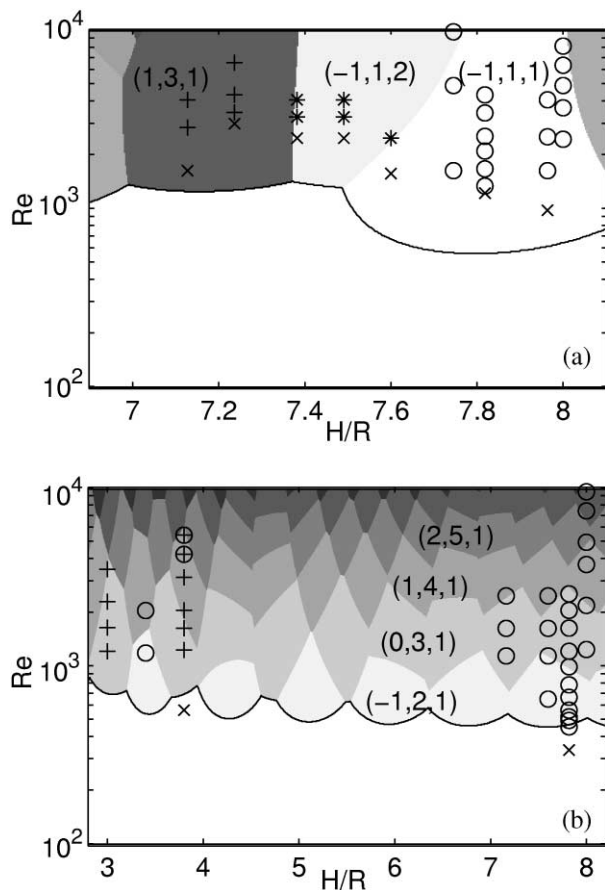
FIG. 7. Comparison between the prediction of the most unstable mode and experimental observations for $n = 2$ (a) and $n = 3$ (b). Each grey tone corresponds to a different mode predicted as labeled. Symbols represent experiments: $\bigcirc$, $(-1, 1, 1)$; $*$, $(-1, 1, 2)$; $+$, $(1, 3, 1)$ in (a) and $\bigcirc$, $(-1, 2, 1)$; $+$, $(0, 3, 1)$ in (b). Symbols ($\times$) correspond to visualizations with no distinct mode.

predictions for principal modes $(-1, 2, 1)$ and $(0, 3, 1)$. The difference of frequencies between these two modes is particularly visible on the spatiotemporal diagrams of the same duration (Figs. 6c and 6d).

The comparison between linear predictions of the most unstable mode and experimental observations is summarized in Fig. 7. For elliptic deformations, the agreement between theory and experiments is excellent, except close to threshold where the instability is not detected by visualizations. This is probably due to the small amplitude of the modes for low Re, in accordance with the supercriticality of the bifurcation [12]. By contrast, for triangular deformations, the agreement between theory and experiment is better close to threshold (Fig. 7b). In the range of aspect ratios studied, the two different modes predicted by the theory have been observed. Note, however that the mode selection is not as sharp as in the elliptic case since, for $H/R > 5.5$, principal mode $(-1, 2, 1)$ is always the

most unstable close to threshold. Interestingly, this particular mode is also observed for larger Re although it does not have the largest growth rate. This could be related to nonlinear effects which are probably also responsible for the puzzling cycle observed between modes $(-1, 2, 1)$ and $(0, 3, 1)$ at $H/R = 3.8$, Re $= 4300$ and 5500 (see Fig. 7b).

The experimental results reported in this letter characterize, for the first time, a large family of multipolar instability modes. In particular, oscillating modes have been evidenced in elliptic and triangular geometries, as predicted by linear stability analysis. These results extend the previous observations which were restricted to steady modes in the elliptic geometry [6,7]. In this case, we have also observed a secondary instability mode, in agreement with recent simulations [12]. For Reynolds numbers below 4000, both primary and secondary instabilities have been visualized in their saturated regimes. Above this value, the vortex breaks up and the flow enters a cycle of disordered and laminar states.

As seen in this Letter, the multipolar instability is very rich. Its diversity makes it a promising mechanism to explain the complex dynamical behavior of vortices in turbulent flows.

[1] O. Cadot, S. Douady, and Y. Couder, Phys. Fluids 7, 630 (1995); J. Jiménez and A. A. Wray, J. Fluid Mech. 373, 255 (1998).

[2] S. Arendt, D. C. Fritts, and Ø. Andreassen, Eur. J. Mech. B, Fluids 17, 595 (1998).

[3] R. T. Pierrehumbert, Phys. Rev. Lett. 57, 2157 (1986); B. J. Bayly, Phys. Rev. Lett. 57, 2160 (1986).

[4] D. W. Moore and P. G. Saffman, Proc. R. Soc. London A 346, 413 (1975); C.-Y. Tsai and S. E. Widnall, J. Fluid Mech. 73, 721 (1976).

[5] H. K. Moffatt, S. Kida, and K. Ohkitani, J. Fluid Mech. 259, 241 (1994).

[6] E. B. Gledzer et al., Izv. Acad. Sci. USSR, Atmos. Oceanic Phys. 11, 617 (1975); E. B. Gledzer and V. M. Ponomarev, J. Fluid Mech. 240, 1 (1992).

[7] W. V. R. Malkus, Geophys. Astrophys. Fluid Dyn. 48, 123 (1989); W. V. R. Malkus and F. A. Waleffe, in Advances in Turbulence III, edited by A. V. Johansson and P. H. Alfredsson (Springer, Berlin, 1991), pp. 197–203.

[8] G. Gauthier, P. Gondret, and M. Rabaud, Phys. Fluids 10, 2147 (1998).

[9] The stream function (1) describes a flow with the largest velocities in the large curvature regions, whereas in the experiment, velocity is uniform on the boundary. This difference is a higher order effect for small ε.

[10] S. Le Dizès and C. Eloy, Phys. Fluids 11, 500 (1999).

[11] C. Eloy and S. Le Dizès (to be published).

[12] R. R. Kerswell, J. Fluid Mech. 382, 283 (1999); D. M. Mason and R. R. Kerswell, J. Fluid Mech. 396, 73 (1999).